Wettability control of droplet durotaxis

Wettability control of droplet durotaxis

Jesus Bueno[1,*], Yuri Bazilevs[2], Ruben Juanes[3], and Hector Gomez[4]

[1]Departamento de Matemáticas, Universidade da Coruña. Campus de Elviña, A Coruña, 15192, Spain
[2]Department of Structural Engineering, University of California, San Diego. 9500 Gilman Drive, La Jolla, CA 92093, USA
[3]Department of Civil and Environmental Engineering, Massachusetts Institute of Technology. 77 Massachusetts Avenue, Cambridge, MA 02139, USA
[4]School of Mechanical Engineering, Purdue University, 585 Purdue Mall, West Lafayette, IN 47907, USA
[*]jesus.bueno@udc.es

ABSTRACT

Durotaxis refers to cell motion directed by stiffness gradients of an underlying substrate. Recent work has shown that droplets also move spontaneously along stiffness gradients through a process reminiscent of durotaxis. Wetting droplets, however, move toward softer substrates, an observation seemingly at odds with cell motion. Here, we extend our understanding of this phenomenon, and show that wettability of the substrate plays a critical role: while wetting droplets move in the direction of lower stiffness[1], nonwetting liquids reverse droplet durotaxis. Our numerical experiments also reveal that Laplace pressure can be used to determine the direction of motion of liquid slugs in confined environments. Our results suggest new ways of controlling droplet dynamics at small scales, which can open the door to enhanced bubble and droplet logic in microfluidic platforms.

Introduction

The ability to generate and manipulate liquid droplets as well as to control how they interact with solid substrates has attracted increased interest in the scientific community due to the number of applications in which droplet dynamics plays a fundamental role. Understanding, predicting and controlling these processes is essential, for example, in the design of new materials and devices at small scales[2–5]; droplets are present in optofluidic optical attenuators[6], microfluidic electronic paper[7] and, in general, in bubble- and droplet-based microfluidic platforms[8–10] that are used for industrial, biological and chemical applications, such as high- and ultrahigh-throughput screening[11–13], enzymatic assays[14] and chemical synthesis[15].

During the past few decades, important advances have been achieved in the study of droplet motion in solid substrates[16–18]. Different mechanisms have been identified and explored to overcome the contact angle hysteresis and induce droplet motion, ranging from the use of chemical, thermal and electrical gradients[19–21] to the manipulation of the surface topography[22] or the application of external vibrations[23]. However, despite significant progress in recent years, droplet motion—especially in relation to deformable substrates—is not fully understood. New mechanisms to control droplet motion on deformable solids have been proposed recently. For example, droplet motion may be driven by gradients in strain of the substrate[24]—a process termed tensotaxis by analogy with the behavior previously observed in cells[25]. Another cell motion mechanism—durotaxis—had already inspired new ways of controlling droplet dynamics: wetting droplets deposited on substrates with nonuniform stiffness tend to move toward the softer parts of the substrate[1]. This directed motion, however, is seemingly opposite to the behavior observed in cells[25].

As it turns out, a central element of droplet durotaxis has heretofore remained unexplored. Here, we show that the behavior of droplets in substrates with nonuniform stiffness depends critically on the wettability of the substrate with respect to the liquid: while wetting droplets move toward the softer parts of the substrate—in agreement with the experiments reported by Style et al.[1]—nonwetting droplets exhibit the opposite behavior and move in the direction of greater stiffness—similarly to the response of cells to rigidity gradients of the underlying substrate[25]. We also elucidate the role of Laplace pressure in this mechanism, and our results suggest that Laplace pressure may be used to control the direction of motion of nonwetting droplets.

This improved understanding of the impact of wetting on droplet durotaxis stems from a computational model of the interaction of deformable solids and multiphase fluids, which accounts for the dynamically coupled, nonlinear problem in three dimensions. The proposed theory allows to make predictions via high-fidelity numerical simulations that elucidate the phenomenon and inform future experimental designs.

Model of droplet durotaxis

When a small liquid droplet is deposited on a flat, rigid and chemically homogeneous solid surface, the droplet tends to adopt a spherical shape and modify its contact angle until it reaches the mechanical equilibrium. The value of the static contact angle α depends on the surface tension at the liquid–vapor γ_{LV}, solid–vapor γ_{SV} and solid–liquid γ_{SL} interfaces, and can be approximated by taking the following balance of forces at the contact line [see Fig. 1(A)],

$$\gamma_{SL} + \gamma_{LV}\cos(\alpha) = \gamma_{SV}. \tag{1}$$

This expression, known as the Young–Dupré equation, has been known for almost two centuries. Equation (1), however, is only valid for ideal solid surfaces, where the solid is flat and infinitely rigid. When the Laplace pressure or the surface tension at the liquid–vapor interface are sufficiently strong so as to deform the substrate, the Young–Drupré equation is no longer valid; see Fig. 1. This may happen for slender structures[26–28] but also when the droplet is small or when it is deposited on a sufficiently soft substrate[29,30]. The elastocapillary length scale $L_{EC} \sim \gamma_{LV}/E$, where E is the substrate's Young modulus, allows to estimate when the elastocapillary forces are relevant and the Young–Dupré equation breaks down.

For most solids and typical values of liquid surface tension, this results in immeasurably small elastocapillary length scales that are much smaller than the radius of the droplet. In these cases, the deformation of the solid is negligible and the Young-Dupré theory is valid. For soft solids such as some gels, however, L_{EC} can approach or even exceed the size of wetting droplets. In such cases, in which small droplets wet soft substrates, the interfacial forces create a ridge at the contact line and the Laplace pressure dimples the substrate under the droplet; see Fig. 1(B). As a consequence, there is a rotation of the contact line[30] and the apparent contact angle, that is, the angle formed by the liquid–vapor interface and the undeformed surface of the substrate (φ in Fig. 1), differs from the angle predicted by the Young–Dupré equation. When a droplet is deposited on a substrate with variable stiffness, the rotation of the contact line—and thus, the apparent contact angle—is different at each side of the droplet, resulting in an imbalance of horizontal forces that may trigger the motion of the droplet.

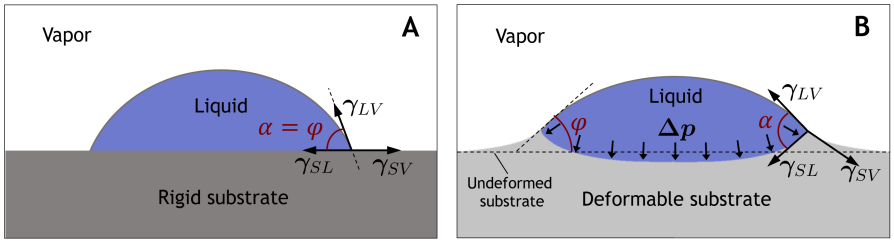

Figure 1. Wetting on rigid and deformable substrates at small scales. (A) Liquid droplet (blue) deposited on a rigid substrate (dark gray). The spherical shape adopted by the droplet depends on the surface tensions at the contact line: γ_{LV}, γ_{SV} and γ_{SL}. The static contact angle α is given by the Young–Dupré equation. (B) Liquid droplet on a soft substrate (light gray). The surface tension at the liquid–vapor interface γ_{LV} creates a ridge at the contact line and the Laplace pressure Δp dimples the substrate under the droplet. The contact lines rotate and thus, the apparent contact angle φ differs from the Young–Dupré contact angle α.

Previous studies of the interaction of droplets and deformable substrates[29,31] are based on linear elastic solids and thin film descriptions of the fluid that allow for the computation of minimum-energy configurations. To advance our understanding of the impact of wettability—especially in the regime of nonwetting droplets—here we propose to model the interaction between droplets and deformable solids using a three-dimensional theory that couples a two-phase fluid with a nonlinear solid. The fluid is composed of a liquid and a gaseous phase separated by a diffuse interface that accurately captures surface tension[32]. The proposed model is solved computationally using a spline-based finite-element method known as isogeometric analysis[33], ideally suited for the simulation of high-order partial differential equations that arise as a result of interfacial effects.

Results

Wettability and droplet durotaxis

The dynamics of wetting droplets ($\alpha < 90°$) on substrates with nonuniform stiffness has been studied previously[30]. However, the role that liquid wettability plays in droplet durotaxis remains unexplored. To study this problem we start by mimicking the experiments conducted by Style et al.[30]. We model a solid substrate (see Fig. 2) composed of two different layers; the lower layer is a rigid material (dark gray) and the upper layer is a deformable solid (light gray). Both materials extend along the solid substrate but their thickness varies in one of the horizontal directions so that the total thickness of the composite substrate

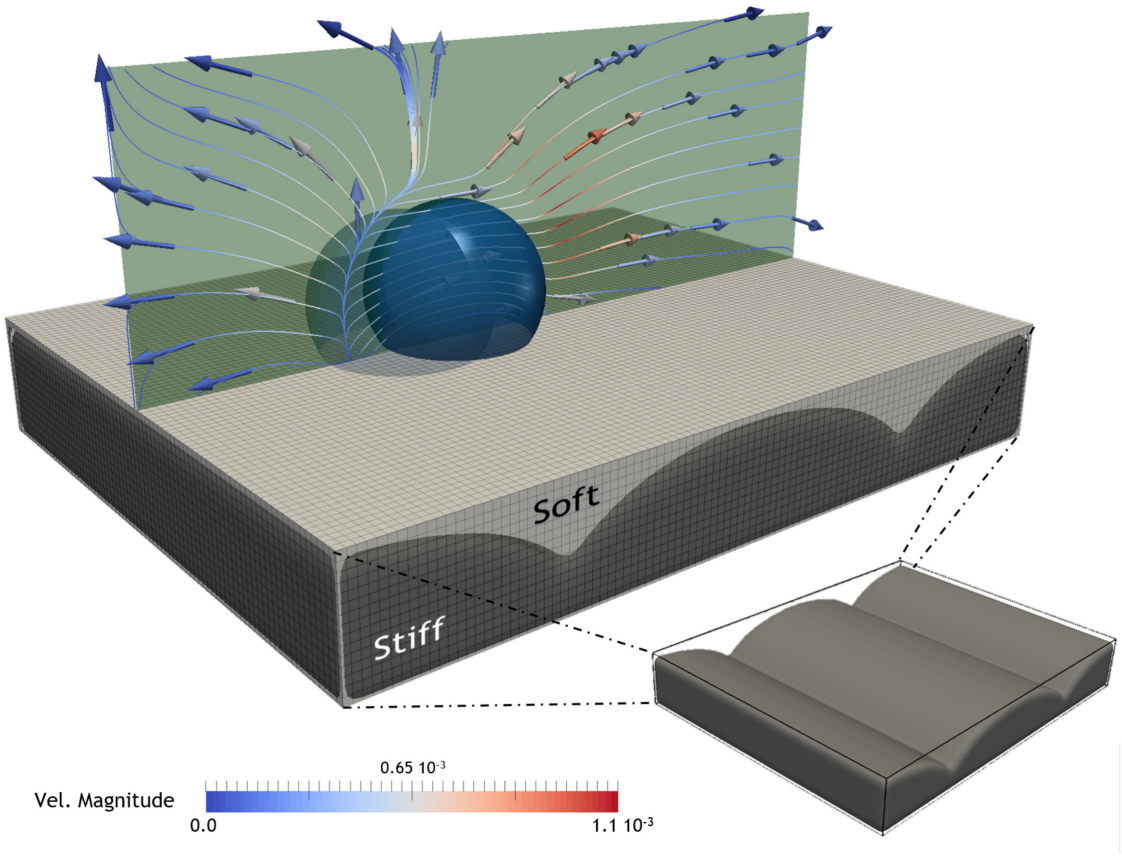

Figure 2. Nonwetting droplets move in the direction of higher stiffness. A liquid droplet (blue) that forms a contact angle of $\alpha = 120^\circ$ with the solid surface is deposited on a substrate with nonuniform stiffness. The substrate is composed of a soft (light gray) and a rigid material (dark gray). The initial position of the droplet is indicated by a semitransparent spherical cap. The droplet moves to the right, where the thickness of the soft material is smaller. We plot the streamlines of the fluid velocity along the mid-plane, which are colored with the velocity magnitude. The computational domain is a box of size $1.0 \times 0.8 \times 0.5$. The computational mesh is comprised of $100 \times 80 \times 50$ $\mathscr{C}^1$-quadratic elements. We have used the parameters $\nu = 0.125$, $\widehat{\mu} = 1/200$, $\widehat{\gamma} = 2/100$, and $\widehat{\theta} = 0.39$. The stiffness of the substrate is $\widehat{E} = 0.42$ in the soft material and $\widehat{E} = 124.2$ in the rigid material. The radius of the droplet is $R = 0.11$. See Methods section for the definition of these quantities.

remains constant. The rigid layer has a lenticular shape (see inset in Fig. 2) and is coated with the deformable solid, creating a flat solid surface. This configuration results in a substrate that has a nonuniform rigidity. The solid is stiffer in the regions where the thickness of the soft material is smaller.

We place a nonwetting droplet ($\alpha = 120^\circ$) on one of the softer regions of the substrate and let the droplet evolve freely in the absence of gravity/external forces. In Fig. 2 we show the configuration of the liquid droplet at time $t = 181$ (the isosurface of dark blue color represents the liquid–vapor interface of the droplet). The initial position of the droplet is indicated in semitransparent light blue color. We also plot the streamlines of the fluid velocity along the mid-plane. The streamlines are colored with the velocity magnitude. The numerical experiment in Fig. 2 shows an important result. The nonwetting droplet advances in the direction of higher stiffness with a time-decreasing velocity; in contrast with what had been observed for wetting droplets. This observation shows that the direction of droplet durotaxis may be reversed by simply altering the wettability of the liquid. To further study the mechanisms of durotaxis, in what follows we adopt a simplified configuration in two dimensions and with solid substrates of constant rigidity gradients.

Mechanistic underpinning of droplet durotaxis

We start by comparing the behavior of wetting and nonwetting droplets on deformable substrates with nonuniform stiffness. We use our nonlinear fluid–structure interaction model to simulate a solid substrate (gray in Fig. 3) with spatially variable stiffness dynamically coupled to a two-phase fluid with surface tension. The rigidity of the substrate follows a linear profile and is lower on the left boundary (light gray) and higher on the right boundary (dark gray) of the solid domain. We place

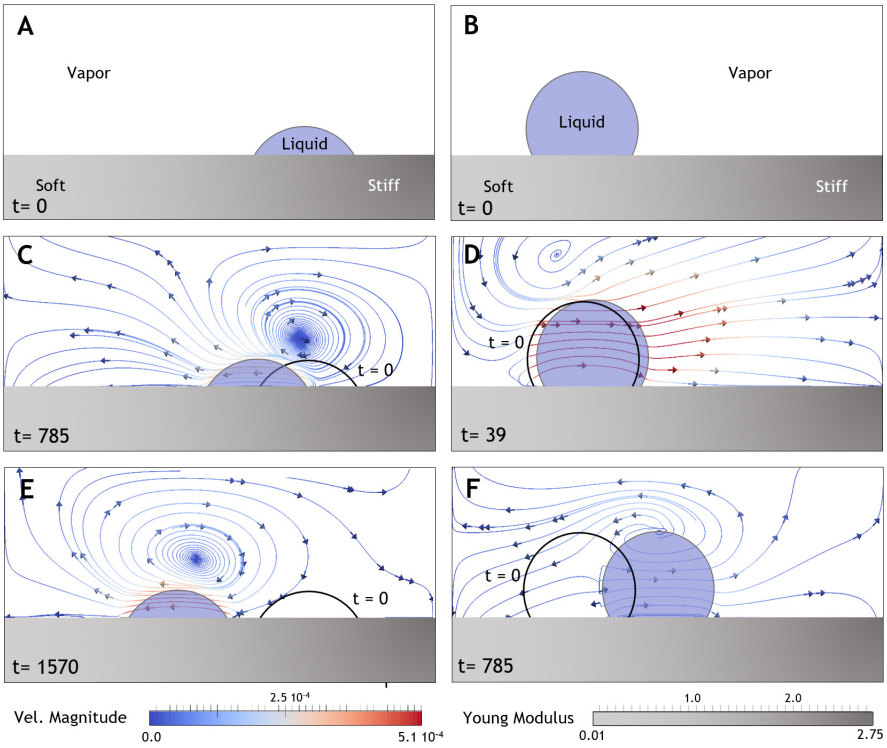

Figure 3. Droplet motion driven by durotaxis. (A) and (B) show the initial configurations: a liquid droplet (blue) is deposited on a substrate (gray) with nonuniform stiffness. On the left column, the droplet initially forms a contact angle of $\alpha = 60^\circ$ with the substrate. On the right column, the droplet is a nonwetting liquid with $\alpha = 120^\circ$. In both cases, the rigidity of the solid follows a linear profile reaching a maximum at the right end. Figs. (C) and (E) show the wetting droplet at two different instants. Figs. (D) and (F) present the time evolution of the nonwetting droplet. The initial position of the droplets is illustrated with a black solid line that represents the liquid–vapor interface at $t = 0$. Figs. (C)–(F) also show the streamlines of the fluid velocity colored by velocity magnitude. The results show that wetting droplets move toward softer parts of the substrate with an increasing velocity magnitude [(C), (E)]. Nonwetting droplets move toward stiffer areas with a decreasing velocity magnitude [(D), (F)]. The computational domain is a box of size 1.0×0.5, discretized with a mesh of 256×128 $\mathscr{C}^2$ elements. The substrate thickness is 0.15 and its Poisson ratio $\nu = 0.125$. The maximum value of the Young modulus is $\widehat{E}_{\max} = 2.75$. The minimum value is $\widehat{E}_{\min} = 0.1$ for the wetting droplet and $\widehat{E}_{\min} = 0.01$ for the non-wetting liquid. For the fluid, we have adopted the parameters, $\widehat{\mu} = 1/512$, $\widehat{\gamma} = 2/256$, and $\widehat{\theta} = 0.39$. The radius of the droplets is $R = 0.13$.

a liquid droplet (blue) on the solid surface and let it move freely in absence of external forces. We analyze the behavior for two different Young–Dupré contact angles. Figs. 3(A) and (B) show the initial configuration of the droplets. The left column in Fig. 3 illustrates the time evolution of a wetting droplet ($\alpha = 60^\circ$), and the right column the corresponding evolution of a nonwetting droplet ($\alpha = 120^\circ$).

The results of our simulations show a remarkable difference in the behavior of wetting and nonwetting droplets, consistent with the three-dimensional results of Fig. 2. While the wetting droplet moves toward the softer part of the substrate, the nonwetting droplet advances in the opposite direction, i.e., it migrates up rigidity gradients. Similar numerical experiments were carried out for other linear stiffness profiles and other values of the Young–Drupré contact angle (data not shown). The results unveiled that the value of the contact angle α for which the direction of the motion is reversed depends on the rigidity of the substrate for a given liquid droplet and Poisson ratio. For the cases that we have analyzed, the motion is reversed for $\alpha \in [105^\circ, 108^\circ]$, where the larger values correspond to stiffer substrates. We have also observed that this value increases with the Poisson ratio.

The streamlines of the fluid velocity, colored by velocity magnitude in Fig. 3, show that droplet motion is able to create a vortical structure in the vapor phase. For the wetting droplet (left column), the magnitude of the droplet velocity increases with time [Fig. 4(A)]. For the nonwetting droplet (right column), the velocity magnitude decreases with time [Fig. 4(B)]. This indicates that droplets move faster in softer areas of substrates with constant stiffness gradients.

The mechanistic explanation for the observed droplet velocity rests on the apparent contact angle at the front and rear

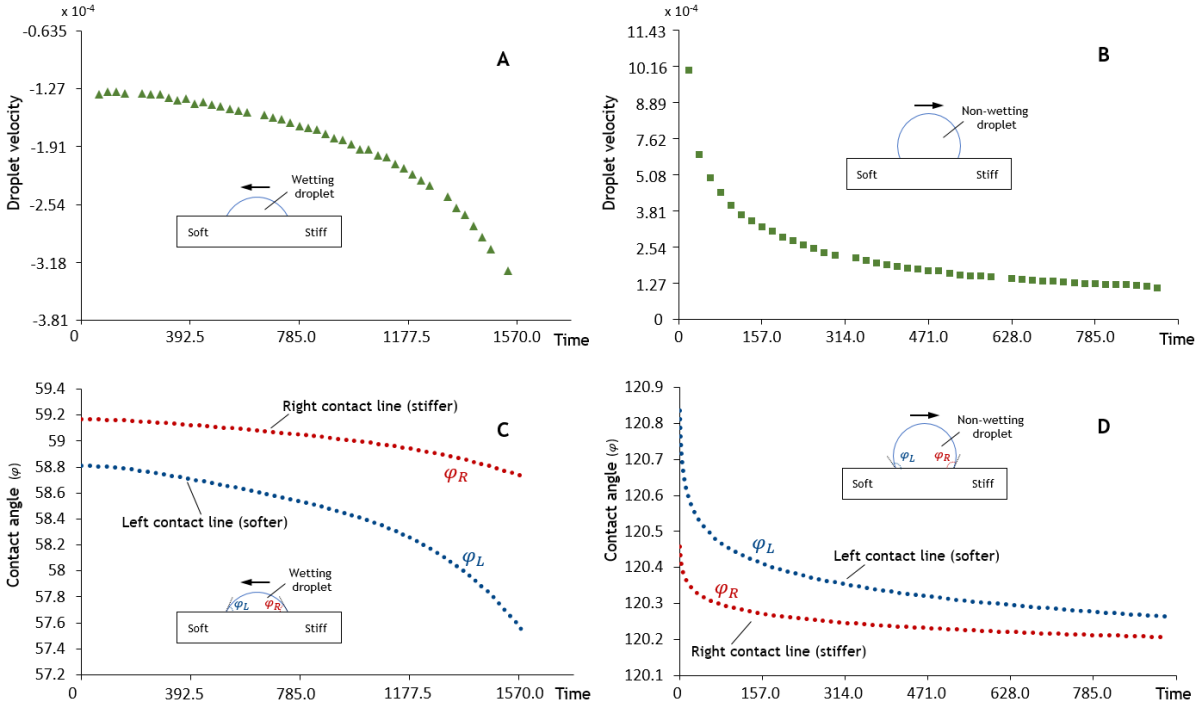

Figure 4. Time evolution of the droplet velocity and the apparent contact angles for the wetting and nonwetting droplets shown in Fig. 3. (A) The wetting droplet moves faster as it advances toward the softer part of the substrate. (B) The nonwetting droplet decelerates as it advances toward the stiffer region. The velocity results are consistent with the evolution of the apparent contact angle difference at both sides of the droplets. (C) and (D) show the time evolution of the apparent contact angles at the front and the rear contact lines. (C) For the wetting droplet, the apparent contact angle on the left (front) side is smaller than the contact angle on the right (rear) contact line. The difference between both contact angles increases as the droplet moves toward the softer area. (D) The nonwetting droplet also moves in the direction of the smaller apparent contact angle (right contact line). As the droplet moves toward the stiffer area, the difference between the front and the rear contact angles decreases.

contact lines of the droplets (relative to the displacement direction); see Figs. 4(C) and (D) for the wetting and nonwetting droplets, respectively. In both cases, the droplet moves toward the contact line in which the apparent contact angle is smaller, that is, the "softer" contact line in wetting droplets and the "stiffer" contact line in nonwetting droplets. For a wetting droplet, the difference between the two apparent contact angles increases with time, as does the velocity magnitude [Fig. 4(A) and (C)]. In contrast, for a nonwetting droplet, the difference between the apparent contact angles at each side of the droplet decreases with time. As the droplet moves to the stiffer region, the surface tension and the Laplace pressure produce a smaller deformation of the substrate and a smaller rotation of the contact line. As a result, the apparent contact angle approaches the static contact angle predicted by Young–Dupré equation. When both rear and front apparent contact angles reach the same value, the droplet stops. These results indicate that the dynamics of the droplets seem to be primarily controlled by the apparent contact angles at opposite sides of the droplet.

The wetting and nonwetting droplets analyzed in these simulations have the same radius and surface tension and, thus, the Laplace pressure is also the same in both cases. If we assume that the droplets have the shape of a circular segment, the distance between the two contact lines will be the same in both cases because the wetting and nonwetting contact angles are supplementary. Since the Laplace pressure takes the same value in both cases and acts on the same length, the contact line rotation produced by the Laplace pressure has the same sign for the wetting and the nonwetting droplet, that is, clockwise for the left contact line and counter-clockwise for the right contact line. Note also that the apparent contact angle is smaller than the Young–Drupré contact angle for wetting droplets [Fig. 4(C)]. For nonwetting droplets, the opposite is true [Fig. 4(D)]. This indicates that the rotation of the contact lines produced by surface tension has different sign for wetting and nonwetting droplets. For example, in the left contact line the rotation seems to be clockwise for wetting droplets and counter-clockwise for nonwetting droplets. This suggests that the rotation induced by the surface tension in nonwetting droplets has opposite sign and greater absolute value than the rotation caused by the Laplace pressure.

To confirm this hypothesis we carried out several computations on substrates with uniform stiffness for a given droplet

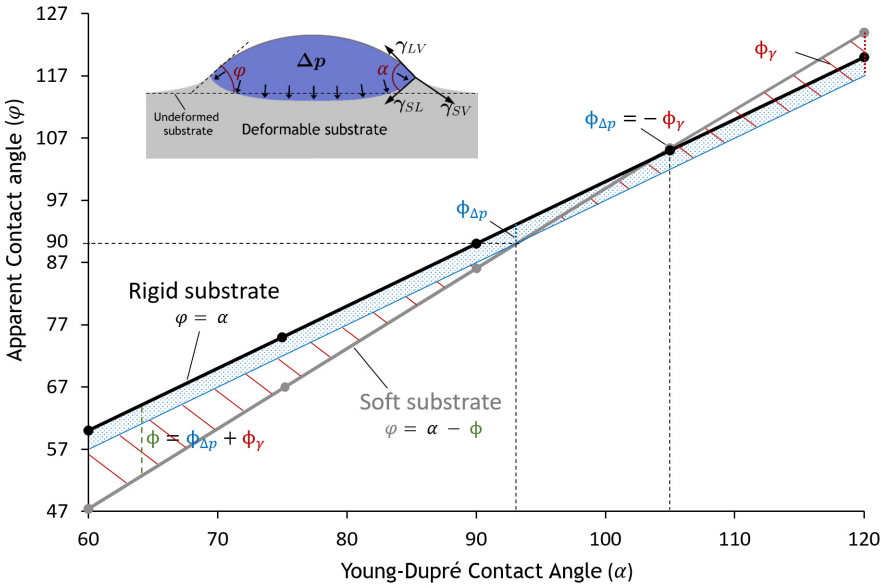

Figure 5. Apparent contact angle φ with respect to the contact angle α predicted by Young–Dupré equation for a given liquid droplet and for substrates of uniform stiffness. In rigid substrates, the deformation produced by surface tension and Laplace pressure is negligible and the apparent contact angle matches the Young–Dupré equilibrium contact angle (black solid line). For sufficiently soft substrates, the Laplace pressure Δp and the surface tension γ_{LV} deform the solid, inducing a rotation ϕ of the contact line (gray solid line). When $\varphi = 90^\circ$, surface tension points vertical and induces no rotation of the contact line, i.e., $\phi_\gamma = 0$. The rotation is entirely produced by the Laplace pressure, i.e., $\phi = \phi_{\Delta p}$, which is constant for all the computations with the same substrate stiffness (blue dotted area). The remaining contribution to the rotation (red striped area) is attributed to surface tension. Note that for $\varphi \simeq 105^\circ$, $\phi_\gamma = -\phi_{\Delta p}$ and the apparent contact angle matches the Young–Dupré contact angle. For $\varphi \gtrsim 105^\circ$, $|\,\phi_\gamma\,| \geq |\,\phi_{\Delta p}\,|$ and the final apparent contact angle exceeds the contact angle predicted by the Young–Dupré equation. The computations were performed on a box of size 1.0×0.5 and using 256×128 $\mathscr{C}^2$ elements. The droplet radius is $R = 0.13$ and the substrate thickness 0.15. We have used the parameters $\nu = 0.125$, $\widehat{E}_{soft} = 0.2$, $\widehat{\mu} = 1/512$, $\widehat{\gamma} = 2/256$, and $\widehat{\theta} = 0.39$.

radius and surface tension; see Fig. 5. We measured the steady-state value of the apparent contact angle φ on a soft substrate (gray solid line) for different Young–Dupré contact angles α. We compared our measurements with the values of φ on a infinitely rigid solid (black solid line). Let us call ϕ_γ and $\phi_{\Delta p}$ the contact line rotations produced by surface tension and Laplace pressure, respectively. The total rotation of the contact line is $\phi = \phi_\gamma + \phi_{\Delta p}$. The results in Fig. 5 confirm that the rotation of the contact line, ϕ, changes sign approximately when $\alpha \simeq 105^\circ$. For $\varphi \gtrsim 105^\circ$, ϕ_γ and $\phi_{\Delta p}$ have opposite sign and $|\,\phi_\gamma\,| > |\,\phi_{\Delta p}\,|$. These observations suggest that a relative increase of the Laplace pressure with respect to surface tension could potentially change the sign of the rotation at the contact lines and thus reverse the direction of droplet motion for nonwetting droplets.

Controlling durotaxis by confinement

To study the role of Laplace pressure in droplet motion driven by durotaxis, we propose a system in which this quantity can be easily manipulated. We place a liquid slug in between two identical planar surfaces forming a capillary bridge (see Fig. 6). In this system, the Laplace pressure scales with the distance between the two solid surfaces. Thus, one can alter the relative strength of the Laplace pressure with respect to surface tension by changing the distance between the solids while keeping the Young–Drupré contact angle α constant.

We carry out two different simulations; see Figs. 6(A) and (B) for the initial configurations. In both cases, the solids have a nonuniform stiffness that follows a linear profile. They are softer on the left boundary (light gray) and stiffer on the right boundary (dark gray). Each simulation has a different distance between the two solids, while the Young–Dupré contact angle is the same for both cases, $\alpha = 120^\circ$, corresponding to a nonwetting liquid slug. For the larger separation between substrates (left column of Fig. 6), the Laplace pressure is lower. In this case, the liquid moves toward the stiffer parts of the substrate. The dynamics seems to be controlled by surface tension. The time evolution of the difference between the apparent contact angles at both sides of the liquid bridge is similar to that observed for the nonwetting droplet analyzed in Fig. 4(D). When the gap between substrates is 10 times smaller (right column of Fig. 6), the Laplace pressure is 10 times larger. In contrast with the

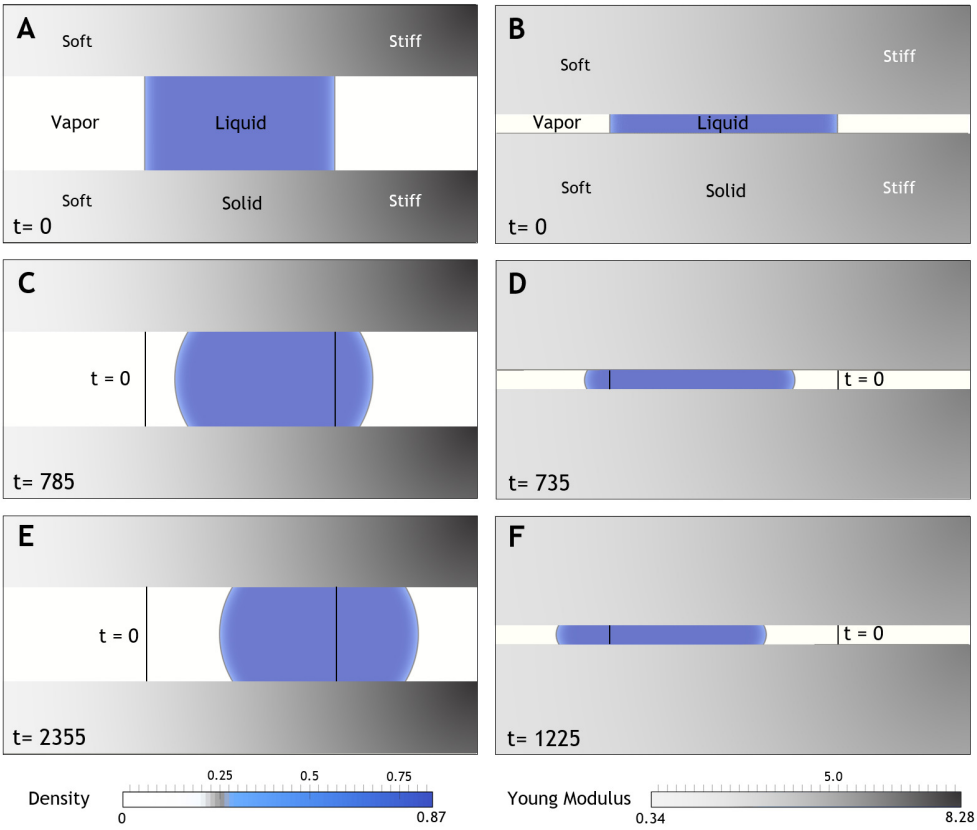

Figure 6. Laplace pressure can be used to alter the direction of confined liquid slugs. A liquid droplet (blue) is placed in between two identical solids (gray) forming a capillary bridge. The solids' stiffness increases linearly from left to right. We analyze two different cases for the same Young-Drupré contact angle ($\alpha = 120°$) and the same surface tension. We do modify the distance between the solids. On the left column the gap is bigger, which results in a lower Laplace pressure. (A) and (B) represent the initial configurations of the problem. (C)-(F) depict the configuration of the capillary bridges at different time instants. The results show that for large Laplace pressures (right column) the droplet moves toward softer regions. For low Laplace pressure, the liquid moves toward stiffer areas. The computational domain is a box of size 1.0×0.5 for the left problem and a box of size 1.0×0.25 for the right problem. They are both discretized with 256×128 $\mathscr{C}^1$ quadratic elements. We use the parameters $\widehat{\mu} = 1/512$, $\widehat{\gamma} = 2/256$, $\widehat{\theta} = 0.39$ and $\nu = 0.125$. The rigidity of the substrate varies linearly between $\widehat{E}_{\min} = 0.34$ and $\widehat{E}_{\max} = 8.28$. The thickness of the solids is 0.15 and 0.115 for the left and the right problems, respectively. Note that for visualization purposes in the right problem we are only showing the central part of the domain.

previous case, here the capillary bridge moves toward the softer part of the solid, showing that durotaxis of liquid slugs can be reversed by judiciously manipulating the Laplace pressure in confined environments.

Discussion

It is generally accepted that, when a droplet is deposited on deformable substrates, the surface tension at the liquid–vapor interface and the Laplace pressure of the droplet produce a rotation of the contact lines[29–31,34]. The numerical experiments conducted here show that this rotation is remarkably different for wetting and nonwetting droplets. While in wetting droplets the rotation induced by the surface tension and the Laplace pressure have the same sign, the opposite is true for nonwetting droplets: the rotation produced by surface tension may outweigh the effect of the Laplace pressure, resulting in apparent contact angles that are larger than the Young–Drupré contact angle. Our results also indicate that the total rotation of the contact line is larger in softer substrates regardless of the wettability of the liquid. These observations explain why in our simulations the apparent contact angle is smaller in the softer part of the substrate for wetting droplets, while the opposite is observed for nonwetting droplets.

Our results support the theory proposed by Style et al.[1] which suggests that–analogously to droplet motion driven by interfacial energy gradients[24]—droplet durotaxis is to a large extent controlled by the difference between the apparent contact

angles at the rear and the front contact lines of the droplet. Droplets move in the direction of the contact line that presents a smaller apparent contact angle. We have shown that for nonwetting droplets this may produce motion toward stiffer areas, mimicking the behavior of cell durotaxis. For wetting droplets, the contact angle difference and the droplet velocity both increase as the droplet moves toward softer areas of the substrate. In contrast, for nonwetting droplets, the contact angle difference and the velocity both decrease as droplets advance toward stiffer areas. Droplets move faster in the softer areas of the substrate for constant stiffness gradients.

Our study opens new possibilities to control the dynamics of droplets in soft substrates. The Laplace pressure may be used to reverse the direction of durotaxis for nonwetting liquid slugs under confinement. Droplet motion can also be controlled by simply altering the total wettability of the liquid, which can be accomplished, e.g., by using surfactants.

Several aspects of droplet durotaxis are still unexplored and should be the focus of future research. The interaction of multiple droplets in substrates with nonuniform stiffness or the influence of variable stiffness gradients in droplet velocity could unveil interesting behavior for a better understanding of this phenomenon. Droplet durotaxis appears to be a powerful way of controlling not only the velocity but the direction of droplet motion.

Methods

We developed a model for the interaction of liquid droplets and deformable substrates, similar to the one presented in Bueno et al.[35]. The model captures the coupling between a nonlinear hyperelastic solid and a multiphase fluid that permits the stable coexistence of a liquid and a gaseous phase separated by a diffuse interface endowed with surface tension.

Solid mechanics

We use the momentum balance equation to describe the behavior of the solid, which in Lagrangian form can be expressed as

$$\rho_0^s \left.\frac{\partial^2 \boldsymbol{u}}{\partial t^2}\right|_{\boldsymbol{X}} = \nabla_{\boldsymbol{X}} \cdot \boldsymbol{P}. \tag{2}$$

Here, $\nabla_{\boldsymbol{X}}$ is the gradient with respect to the material coordinates $\boldsymbol{X}$ and $|_{\boldsymbol{X}}$ indicates that the time derivative is taken by holding $\boldsymbol{X}$ fixed; $\boldsymbol{u}$ is the solid displacement and ρ_0^s is the mass density in the initial configuration; $\boldsymbol{P}$ is the first Piola–Kirchhoff stress tensor. As constitutive theory we adopt a nonlinear hyperelastic material. We use the generalized neo-Hookean model with dilatational penalty proposed by Simo and Hughes[36]. In this model, the second Piola–Kirchhoff stress tensor can be defined as

$$\boldsymbol{S} = \mu J^{-2/d}\left(\boldsymbol{I} - \frac{1}{d}\mathrm{tr}(\boldsymbol{C})\boldsymbol{C}^{-1}\right) + \frac{\kappa}{2}\left(J^2 - 1\right)\boldsymbol{C}^{-1}, \tag{3}$$

where $\boldsymbol{I}$ represents the identity tensor, d denotes the number of spatial dimensions and $\mathrm{tr}(\cdot)$ stands for the trace operator; κ and μ are the material bulk and shear moduli, which are expressed as a function of the Young modulus E and the Poisson ratio ν using the relations $\kappa = E/(3(1-2\nu))$ and $\mu = E/(2(1+\nu))$; J is the determinant of the deformation gradient, that is, $J = \det(\boldsymbol{F})$, where $\boldsymbol{F} = \boldsymbol{I} + \nabla_X \boldsymbol{u}$. $\boldsymbol{C}$ denotes the Cauchy–Green deformation tensor, i.e., $\boldsymbol{C} = \boldsymbol{F}^T\boldsymbol{F}$. The first Piola–Kirchhoff stress tensor is obtained by taking $\boldsymbol{P} = \boldsymbol{F}\boldsymbol{S}$. The solid Cauchy stress tensor can be computed using $\boldsymbol{\sigma}^s = J^{-1}\boldsymbol{F}\boldsymbol{S}\boldsymbol{F}^T = J^{-1}\boldsymbol{P}\boldsymbol{F}^T$.

Fluid mechanics

The behavior of the fluid is described by the isothermal form of the Navier–Stokes–Korteweg (NSK) equations. The NSK system constitutes the most widely accepted theory for the description of single-component two-phase flows and it naturally allows for phase transformations in the fluid due to pressure and/or temperature variations. Since we are only interested in studying droplet motion on solid substrates, we select a parameter regime in which mass transfer between the liquid and gaseous phase is negligible. Our approach is based on the diffuse-interface or phase-field method[32], i.e., an alternative to sharp-interface models in which interfaces are replaced by thin transition regions. This allows an efficient computational treatment of the coupled multiphysics problem. In the Eulerian description, the NSK equations can be expressed as

$$\frac{\partial \rho}{\partial t} + \nabla \cdot (\rho \boldsymbol{v}) = 0, \tag{4a}$$

$$\frac{\partial (\rho \boldsymbol{v})}{\partial t} + \nabla \cdot (\rho \boldsymbol{v} \otimes \boldsymbol{v}) - \nabla \cdot \boldsymbol{\sigma}^f = 0, \tag{4b}$$

where $\otimes$ represents the outer vector product, ρ is the fluid density and $\boldsymbol{v}$ denotes the velocity vector. $\boldsymbol{\sigma}^f$ is the Cauchy stress tensor of the fluid, i.e., $\boldsymbol{\sigma}^f = \boldsymbol{\tau} - p\boldsymbol{I} + \boldsymbol{\varsigma}$. Here, $\boldsymbol{\tau}$ stands for the viscous stress tensor, p denotes the pressure, and $\boldsymbol{\varsigma}$ is known as the Korteweg tensor. We consider Newtonian fluids, so the viscous stress tensor takes the form

$$\boldsymbol{\tau} = \bar{\mu}\left(\nabla \boldsymbol{v} + \nabla^T \boldsymbol{v}\right) + \bar{\lambda}\nabla \cdot \boldsymbol{v}\boldsymbol{I}, \tag{5}$$

where $\bar{\mu}$ and $\bar{\lambda}$ are the viscosity coefficients. We assume that the Stokes hypothesis is satisfied, that is, $\bar{\lambda} = -2\bar{\mu}/3$. In order to allow for the stable coexistence of liquid and gas phases we derive the thermodynamic pressure from the Helmholtz free-energy of a van der Waals fluid[37,38]. The resulting van der Waals equation is expressed as

$$p = Rb\left(\frac{\rho\theta}{b-\rho}\right) - a\rho^2, \tag{6}$$

and gives the pressure p in terms of density and temperature θ. a and b are positive constants and R is the specific gas constant. The Korteweg tensor[39,40] is defined by

$$\boldsymbol{\varsigma} = \lambda\left(\rho\Delta\rho + \frac{1}{2}|\nabla\rho|^2\right)\boldsymbol{I} - \lambda\nabla\rho\otimes\nabla\rho. \tag{7}$$

where $\lambda > 0$ is the capillarity coefficient and $|\cdot|$ denotes the Euclidean norm of a vector. The Korteweg tensor gives rise to the capillary forces that are withstood by the liquid–vapor interfaces.

For the fluid problem we adopt the classical solid-wall boundary conditions. Additionally, the third-order partial spatial derivatives of the fluid equations require an extra condition to render a well-posed boundary value problem. To do so, we impose $\nabla\rho\cdot\boldsymbol{n}^f = |\nabla\rho|\cos\alpha$, where $\boldsymbol{n}^f$ is the unit outward normal to the fluid boundary, and α is the contact angle between the liquid–vapor interface and the solid surface (see Fig. 1). Note that this boundary condition allows the imposition of the contact angle α at the fluid–structure interface. The apparent contact angle φ, however, is determined as part of the solution of the problem.

Coupled problem

The partial differential equations and boundary conditions associated with the fluid and structure problems must be satisfied simultaneously. The two systems are coupled at the fluid-–structure interface in order to ensure compatible kinematics ($\boldsymbol{v} = \partial\boldsymbol{u}/\partial t$) and transmission of tractions ($\boldsymbol{\sigma}^f\boldsymbol{n}^f - \boldsymbol{\sigma}^s\boldsymbol{n}^f = 0$) between the fluid and solid domains.

Computational method

We solve the coupled system consisting of Eq. (2) and Eq. (4) subject to the kinematic compatibility and traction balance constraints. Equation (2) is solved in the reference (undeformed) configuration of the solid domain. Equation (4) is solved in the spatial domain occupied by the fluid, which changes over time. This requires the use of geometrically flexible algorithms, such as the finite element method. Here, we use isogeometric analysis, which is a spline-based finite-element-like method that combines geometric flexibility with smooth basis functions[33,41]. The use of smooth basis functions allows for a direct discretization of higher-order partial differential equations such as the NSK equation. To enable the use of classical finite-difference-type methods for time integration, we recast the NSK equations in an arbitrary Lagrangian Eulerian (ALE) formulation:

$$\left.\frac{\partial\rho}{\partial t}\right|_{\widehat{\boldsymbol{x}}} + \left(\boldsymbol{v} - \widehat{\boldsymbol{v}}\right)\cdot\nabla\rho + \rho\nabla\cdot\boldsymbol{v} = 0, \tag{8a}$$

$$\rho\left.\frac{\partial\boldsymbol{v}}{\partial t}\right|_{\widehat{\boldsymbol{x}}} + \rho\left(\boldsymbol{v} - \widehat{\boldsymbol{v}}\right)\cdot\nabla\boldsymbol{v} - \nabla\cdot\boldsymbol{\sigma}^f = 0. \tag{8b}$$

Here, $\widehat{\boldsymbol{v}}$ is the fluid domain velocity and $\widehat{\boldsymbol{x}}$ is a coordinate in a reference domain that is used for computational purposes. Equations (2) and (8) can then be written in variational form and discretized in space using isogeometric analysis. We use the generalized–α method[42] as a time integration scheme. The nonlinear system of equations is solved using a Newton–Raphson iteration procedure, which leads to a two-stage predictor–multicorrector algorithm. The resulting linear system is solved using a preconditioned GMRES method.

We express the problem in nondimensional form by rescaling the units of measurement of time, length, mass and temperature by $L_0/\sqrt{ab}$, L_0, bL_0^3 and θ_c, respectively. Here, $L_0 = 1$ is a length scale of the computational domain and $\theta_c = 8ab/(27R)$ is the so-called critical temperature. Using this nondimensionalization, the problem can be characterized by five dimensionless numbers, i.e., the Poisson ratio ν and the dimensionless Young modulus $\widehat{E} = E/(\rho_0^s ab)$ for the solid problem and the dimensionless surface tension $\widehat{\gamma} = \sqrt{\lambda/a}/L_0$, viscosity $\widehat{\mu} = \bar{\mu}/(L_0 b\sqrt{ab})$ and temperature $\widehat{\theta} = \theta/\theta_c$ for the fluid equations.

References

1. Style, R. W. *et al.* Patterning droplets with durotaxis. *Proc. Natl. Acad. Sci.* **110**, 12541–12544 (2013).
2. De Volder, M. & Hart, A. J. Engineering hierarchical nanostructures by elastocapillary self-assembly. *Angewandte Chemie Int. Ed.* **52**, 2412–2425 (2013).

3. Tawfick, S. H., Bico, J. & Barcelo, S. Three-dimensional lithography by elasto-capillary engineering of filamentary materials. *MRS Bull.* **41**, 108–114 (2016).

4. Raccurt, O., Tardif, F., d'Avitaya, F. A. & Vareine, T. Influence of liquid surface tension on stiction of SOI MEMS. *J. Micromechanics Microengineering* **14**, 1083 (2004).

5. Tanaka, T., Morigami, M. & Atoda, N. Mechanism of resist pattern collapse during development process. *Jpn. J. Appl. Phys.* **32**, 6059 (1993).

6. Monat, C., Domachuk, P. & Eggleton, B. Integrated optofluidics: A new river of light. *Nat. Photonics* **1**, 106–114 (2007).

7. Drzaic, P. Displays: Microfluidic electronic paper. *Nat. Photonics* **3**, 248–249 (2009).

8. Prakash, M. & Gershenfeld, N. Microfluidic bubble logic. *Sci.* **315**, 832–835 (2007).

9. Cira, N. J., Benusiglio, A. & Prakash, M. Vapour-mediated sensing and motility in two-component droplets. *Nat.* **519**, 446–450 (2015).

10. Cueto-Felgueroso, L. & Juanes, R. A phase-field model of two-phase hele-shaw flow. *J. Fluid Mech.* **758**, 522–552 (2014).

11. Fallah-Araghi, A., Baret, J.-C., Ryckelynck, M. & Griffiths, A. D. A completely in vitro ultrahigh-throughput droplet-based microfluidic screening system for protein engineering and directed evolution. *Lab on a Chip* **12**, 882–891 (2012).

12. Agresti, J. J. *et al.* Ultrahigh-throughput screening in drop-based microfluidics for directed evolution. *Proc. Natl. Acad. Sci.* **107**, 4004–4009 (2010).

13. Prakadan, S. M., Shalek, A. K. & Weitz, D. A. Scaling by shrinking: empowering single-cell'omics' with microfluidic devices. *Nat. Rev. Genet.* **18**, 345–361 (2017).

14. Huebner, A. *et al.* Static microdroplet arrays: a microfluidic device for droplet trapping, incubation and release for enzymatic and cell-based assays. *Lab on a Chip* **9**, 692–698 (2009).

15. Song, H., Chen, D. L. & Ismagilov, R. F. Reactions in droplets in microfluidic channels. *Angewandte Chemie Int. Ed.* **45**, 7336–7356 (2006).

16. de Gennes, P., Brochard-Wyart, F. & Quere, D. *Capillarity and Wetting Phenomena: Drops, Bubbles, Pearls, Waves* (Springer New York, 2003).

17. David, B. *Droplet Wetting and Evaporation* (Academic Press, Oxford, 2015).

18. Alizadeh Pahlavan, A., Cueto-Felgueroso, L., McKinley, G. & Juanes, R. Thin films in partial wetting: Internal selection of contact-line dynamics. *Phys. Rev. Lett.* **115**, 034502 (2015).

19. Brochard, F. Motions of droplets on solid surfaces induced by chemical or thermal gradients. *Langmuir* **5**, 432–438 (1989).

20. Wong, P. K., Wang, T.-H., Deval, J. H. & Ho, C.-M. Electrokinetics in micro devices for biotechnology applications. *IEEE/ASME Transactions on Mechatronics* **9**, 366–376 (2004).

21. Pollack, M. G., Fair, R. B. & Shenderov, A. D. Electrowetting-based actuation of liquid droplets for microfluidic applications. *Appl. Phys. Lett.* **77**, 1725–1726 (2000).

22. Fang, G., Li, W., Wang, X. & Qiao, G. Droplet motion on designed microtextured superhydrophobic surfaces with tunable wettability. *Langmuir* **24**, 11651–11660 (2008).

23. Daniel, S., Chaudhury, M. K. & De Gennes, P.-G. Vibration-actuated drop motion on surfaces for batch microfluidic processes. *Langmuir* **21**, 4240–4248 (2005).

24. Bueno, J., Bazilevs, Y., Juanes, R. & Gomez, H. Droplet motion driven by tensotaxis. *Extrem. Mech. Lett.* **13**, 10–16 (2017).

25. Lo, C.-M., Wang, H.-B., Dembo, M. & Wang, Y.-l. Cell movement is guided by the rigidity of the substrate. *Biophys. J.* **79**, 144–152 (2000).

26. Duprat, C., Protiere, S., Beebe, A. Y. & Stone, H. A. Wetting of flexible fibre arrays. *Nat.* **482**, 510–513 (2012).

27. Duprat, C., Bick, A. D., Warren, P. B. & Stone, H. A. Evaporation of drops on two parallel fibers: Influence of the liquid morphology and fiber elasticity. *Langmuir* **29**, 7857–7863 (2013).

28. Roman, B. & Bico, J. Elasto-capillarity: deforming an elastic structure with a liquid droplet. *J. Physics: Condens. Matter* **22**, 493101 (2010).

29. Style, R. W. & Dufresne, E. R. Static wetting on deformable substrates, from liquids to soft solids. *Soft Matter* **8**, 7177–7184 (2012).

30. Style, R. W. *et al.* Universal deformation of soft substrates near a contact line and the direct measurement of solid surface stresses. *Phys. Rev. Lett.* **110**, 066103 (2013).

31. Karpitschka, S. *et al.* Liquid drops attract or repel by the inverted Cheerios effect. *Proc. Natl. Acad. Sci.* **113**, 7403–7407 (2016).

32. Gomez, H. & van der Zee, K. *Encyclopedia of Computational Mechanics. Computational Phase-field Modeling* (John Wiley & Sons, Ltd, 2016).

33. Cottrell, J., Hughes, T. & Bazilevs, Y. *Isogeometric Analysis: Toward Integration of CAD and FEA* (Wiley, 2009).

34. Pericet-Cámara, R., Best, A., Butt, H.-J. & Bonaccurso, E. Effect of capillary pressure and surface tension on the deformation of elastic surfaces by sessile liquid microdrops: an experimental investigation. *Langmuir* **24**, 10565–10568 (2008).

35. Bueno, J., Bona-Casas, C., Bazilevs, Y. & Gomez, H. Interaction of complex fluids and solids: Theory, algorithms and application to phase-change-driven implosion. *Comput. Mech.* **55**, 1105–1118 (2015).

36. Simo, J. & Hughes, T. *Computational Inelasticity* (Springer-Verlag, New Yoirk, 1998).

37. Diehl, D. *Higher order schemes for simulation of compressible liquid-vapor flows with phase change*. Ph.D. thesis, Albert-Ludwigs-Universitat (2007).

38. Liu, J., Landis, C. M., Gomez, H. & Hughes, T. J. Liquid-vapor phase transition: Thermomechanical theory, entropy stable numerical formulation, and boiling simulations. *Comput. Methods Appl. Mech. Eng.* **297**, 476–553 (2015).

39. Korteweg, D. J. Sur la forme que prennent les équations du mouvement des fluides si l'on tient compte des forces capillaires causées par des variations de densité considérables mais continues et sur la théorie de la capillarité dans l'hypothese d'une variation continue de la densité. *Arch. Néerlandaises des Sci. exactes et naturelles* **6**, 6 (1901).

40. Dunn, J. & Serrin, J. On the thermomechanics of interstitial working. *Arch. for Ration. Mech. Analysis* **88**, 95–133 (1985).

41. Hughes, T., Cottrell, J. & Bazilevs, Y. Isogeometric Analysis: CAD, Finite Elements, NURBS, exact geometry and mesh refinement. *Comput. Methods Appl. Mech. Eng.* **194**, 4135–4195 (2005).

42. Chung, J. & Hulbert, G. A time integration algorithm for structural dynamics with improved numerical dissipation: The generalized-α method. *J. Appl. Mech.* **60**, 371–375 (1993).

Acknowledgements

HG was partially supported by the European Research Council through the FP7 Ideas Starting Grant Program (Contract #307201). HG and JB were partially supported by Xunta de Galicia, co-financed with FEDER funds. JB is grateful to the Ph.D. student grant UDC-Inditex for the financial support during his visit at the University of California, San Diego, where part of this work was conducted. **YB ...** RJ acknowledges funding from the U.S. Department of Energy through a DOE Mathematical Multifaceted Integrated Capability Center Award (Grant No. DE-SC0009286).

Author contributions statement

HG and JB conceived the project and led the research process; JB developed the code and performed the numerical experiments; HG and JB carried out most of the theoretical analysis and wrote the manuscript. RJ and YB jointly contributed the ideas and discussed the results. All authors reviewed the manuscript.

Additional information

Competing financial interests The authors declare that they have no competing interests.